Check for updates

From Thermoelectric Powder Directly to Thermoelectric Generators: Flexible Bi$_2$Te$_3$ Films on Polymer Sheets Prepared by the Powder Aerosol Deposition Method at Room Temperature

Robin Werner,* Johanna S. Matejka, Daniela Schönauer-Kamin, and Ralf Moos

The powder aerosol deposition (PAD) method is a spray-coating process to form dense, nanocrystalline ceramic films at room temperature without thermal treatment. Herein, the thermoelectric properties of PAD-deposited Bi$_2$Te$_3$ films are investigated. The powders are deposited on rigid Al$_2$O$_3$ substrates and on flexible polymer sheets (Kapton and Mylar) attached to Kanthal foils. A low thermal conductivity of $\lambda = 0.12 \, \text{W m}^{-1} \, \text{K}^{-1}$, an electrical conductivity of $\sigma = 29.8 \, \text{S cm}^{-1}$, and a Seebeck coefficient of $S = -145 \, \mu\text{V K}^{-1}$ are determined on Al$_2$O$_3$. To evaluate the flexibility of the Bi$_2$Te$_3$ films deposited on flexible polymer sheets, the electrical conductivity and the Seebeck coefficient are measured before, during, and again after bending. While the Seebeck coefficient remains unaffected by the bending process and the bending radius, the electrical conductivity deteriorates to some extent during bending. Subsequent measurements in the nonbent planar state reveal, however, that the conductivity is restored partially. Furthermore, first, flexible thermoelectric generators could be prepared and characterized. PAD offers enormous potential not only in the combination of Bi$_2$Te$_3$ films on polymer sheets without thermal treatment, but also for manufacturing flexible thermoelectric generators in general.

1. Introduction

1.1. Motivation

Thermoelectric generators (TEGs) convert thermal energy directly into electrical energy when a temperature gradient is present.[1–4] In addition to high reliability and low maintenance efforts, they are noiseless and durable. They are therefore already applied in specialized fields such as aerospace engineering.[5–7] Furthermore, the automotive industry is to recover energy from hot exhaust gas using TEGs.[8–11] In parallel to the use of waste heat from technical applications, the use of natural heat dissipation of humans is of increasing interest of research. A strong growth in this sector, especially in the field of smart textiles and wearables, is predicted.[12] However, near-body and wearable TEGs are challenging. In this case, the generators should be as flexible as possible and it should be possible to operate them at room temperature. Today's most common and most efficient material compounds for use in TEGs at room temperature are based on the semiconducting bismuth telluride (Bi$_2$Te$_3$) with a figure of merit ZT of ≈ 1.[13–15] The manufacturing of rigid Bi$_2$Te$_3$ bulk devices is time-, cost-, and energy-intensive and, therefore, limits the applications of TEGs. Flexible and thinner wearable TEGs would enable a wider range of applications and thus entirely new fields of applications.[16–24] Some previous studies manufactured flexible TEGs with polymer-based thermoelectric materials. However, their low electrical conductivities yield low efficiencies.[17,18,25–27]

Powder aerosol deposition (PAD) (often also referred to as aerosol deposition method) is a method for preparing dense metallic or ceramic films at room temperature.[28–30] The films are produced directly from the starting powders. They adhere well and are already dense without a subsequent thermal treatment. This process allows for coating of temperature-sensitive substrates such as polymer films, in addition to metallic, ceramic, and glass substrates. The thicknesses of the nanocrystalline films are in the order of a few micrometers, reducing the overall component thickness of the TEG and saving expensive thermoelectric material. The nanocrystalline film morphology, a typical feature of PAD, leads to the reduction of thermal conductivity and increases the efficiency of the thermoelectric materials.[28,31] Therefore, PAD offers an enormous potential for the manufacture of TEGs.

R. Werner, J. S. Matejka, D. Schönauer-Kamin, R. Moos
Department of Functional Materials
Zentrum für Energietechnik (ZET)
University of Bayreuth
95440 Bayreuth, Germany
E-mail: functional.materials@uni-bayreuth.de

The ORCID identification number(s) for the author(s) of this article can be found under https://doi.org/10.1002/ente.202101091.

**ADVANCED
SCIENCE NEWS**

www.advancedsciencenews.com

Energy Technology
Generation, Conversion, Storage, Distribution

www.entechnol.de

1.2. Research Objectives and Experimental Approach

The aim of this work is to manufacture thermoelectric Bi_2Te_3 films on flexible polymer sheets using the PAD method. Consequently, the good thermoelectric properties of Bi_2Te_3 could be combined with flexible polymer sheets. The fabrication of crystalline, Bi_2Te_3-based flexible TEGs could combine high thermoelectric efficiencies with a wider field of applications.

The experimental approach in this work can be divided into five steps. First, Bi_2Te_3 is deposited on alumina. This step includes optical characterization of the deposited films, phase analysis, and complete thermoelectric characterization, including electrical conductivity σ, charge carrier density n, Hall mobility μ_H, Seebeck coefficient S, and thermal conductivity λ. In the second step, Bi_2Te_3 is deposited on flexible polymer sheets. Self-adhesive Mylar and Kapton with thicknesses of 100 μm each were chosen, which were bonded to 100 μm thin metallic Kanthal foils in advance.

The third step involves the characterization of the electrical conductivity and the Seebeck coefficient of Bi_2Te_3 on flexible substrates not only in the planar state, but also during bending, as well as a further measurement in the planar state after bending. As shown in **Figure 1**, a distinction is made between measurements during bending and before/after bending. In the first part of the experiments with flexible substrates, the thermoelectric behavior of the processed Bi_2Te_3 films during bending is investigated. The manufactured samples are first measured in the planar, nonbent state and then measured during bending and finally examined again in the planar state. The measurements for this are carried out on four convex radii (60/40/20/10 mm), with a

new sample in each case. As the electrical conductivities of the films vary slightly, the initial conductivity is determined for each sample and the changes in conductivity due to the bending load are evaluated in relation to initial conductivity. For the Seebeck coefficient measurements, an external modulation heater is used to generate a variable temperature difference over the Bi_2Te_3 films. Au–Pt thermocouples allow for measuring the contact-point temperature and the thermovoltage between these to determine the Seebeck coefficient. In the second part of the experiments, the behavior after multiple bendings is investigated. For this purpose, a sample is bent up to 20 times over one of the previously mentioned radii and characterized in the planar state, both before and after multiple bendings. In the fourth step, the results will be discussed and evaluated to subsequently prepare a first flexible TEG with Bi_2Te_3 on polymer sheets using the powder aerosol deposition method (PADM). The TEG will be characterized in the plane state before, during bending, and after bending in the plane state again (Step 5).

2. Experimental Section

2.1. The PAD Method

The PAD method is a spray-coating process to generate dense, nanocrystalline ceramic films at room temperature without a thermal treatment. The resulting PAD-films have bulk-like properties without or after very mild thermal annealing,[32] which allows for coating temperature-sensitive substrates such as polymers.
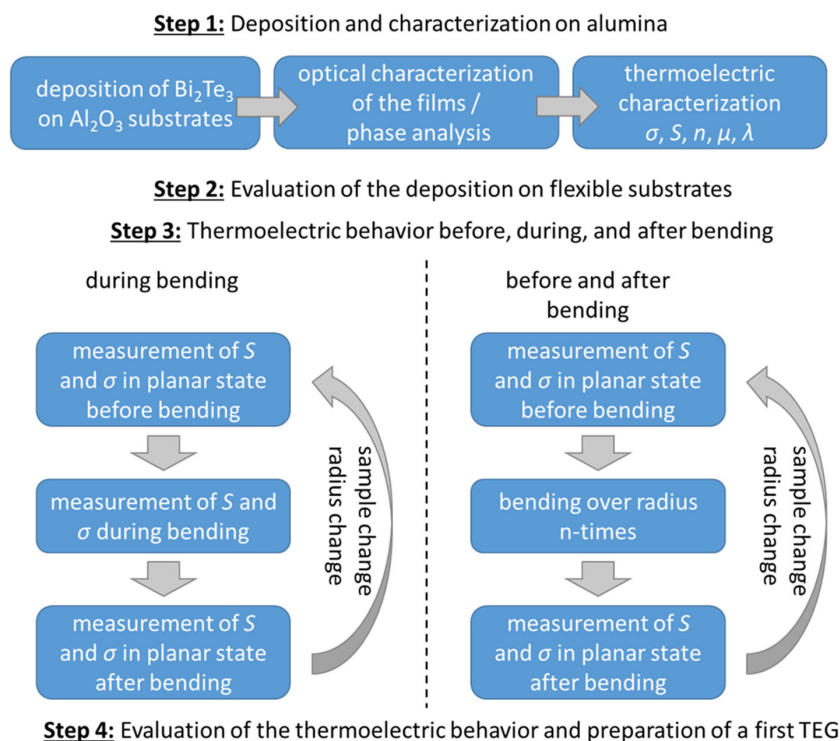

Step 1: Deposition and characterization on alumina

deposition of Bi_2Te_3 on Al_2O_3 substrates → optical characterization of the films / phase analysis → thermoelectric characterization σ, S, n, μ, λ

Step 2: Evaluation of the deposition on flexible substrates

Step 3: Thermoelectric behavior before, during, and after bending

during bending

measurement of S and σ in planar state before bending → measurement of S and σ during bending → measurement of S and σ in planar state after bending

sample change radius change

before and after bending

measurement of S and σ in planar state before bending → bending over radius n-times → measurement of S and σ in planar state after bending

sample change radius change

Step 4: Evaluation of the thermoelectric behavior and preparation of a first TEG

Figure 1. The five steps of the experimental approach of this research.

**ADVANCED
SCIENCE NEWS**

www.advancedsciencenews.com

Energy Technology
Generation, Conversion, Storage, Distribution
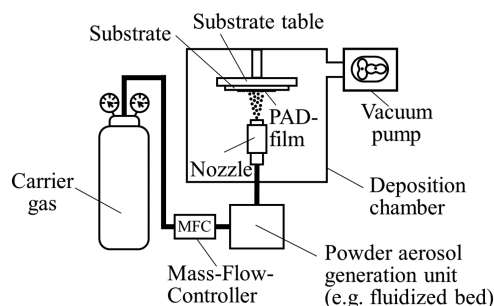
www.entechnol.de

Figure 2. Schematic representation of a PAD setup with aerosol chamber, gas connection, and deposition chamber. Reproduced under terms of the CC-BY license.[30] Copyright 2019, The Authors, published by World Scientific Publishing Company.

99.9% Bi_2Te_3 powder (American Elements, Los Angeles, USA) was used in this work. The dried powder was sieved (mesh size of 90 μm) and then processed directly by PAD. The experimental setup can be seen in **Figure 2**.

The powder was aerosolized (aerosol generator) and accelerated by passing the orifice of a nozzle and was injected into the so-called deposition chamber. The to-be-coated substrate was located on a movable stage. The film formation followed the so-called room-temperature impact consolidation (RTIC) mechanism.[29] The defined geometries were produced via masks that were subsequently removed after coating. A comprehensive description of the PAD process can be obtained from the overviews.[28,29]

2.2. Characterization of the Obtained Films

To compare the crystalline phases of the deposited PAD films with the initial powder, Bi_2Te_3 was deposited on 96% Al_2O_3 (Rubalit 708 S, CeramTec, Marktredwitz, Germany) and then analyzed by X-ray powder diffractometry (XRD, Bruker D8 ADVANCE, Karlsruhe, Germany). The samples were measured with a step size of 0.02°, a measurement time of 0.5 s per step, and a wavelength of 1.54 Å (Cu-Anode 2.2 kW, Ge Kα1-monochromator, 1D-Lynxeye-detector). In addition, scanning electron microscope images were taken from cross sections and surfaces (LEO Gemini1530, Carl Zeiss AG, Oberkochen, Germany). Film thicknesses were measured using a Waveline W20 perthometer (Jenoptik, Jena, Germany).

2.3. Thermoelectric Characterization

For initial characterization of the electrical transport properties of the PAD Bi_2Te_3 films on Al_2O_3, the electrical conductivity σ as well as the charge carrier density n and the mobility μ were measured (Hall-Effect Characterization System HCS 1, Linseis Thermal Analysis, Selb, Germany). A plane-square sample with an edge length of 10 mm was contacted at the corners via infinitesimally small electrodes according to the van der Pauw method. The Hall constant was determined in magnetic fields with a flux density of ±760 mT. A detailed description of the setup can be obtained from the study by Werner et al.[33] The Seebeck coefficient S was measured in a further developed

sample holder of the Hall coefficient measurement setup. The sample holder was extended by two gold–platinum thermocouples for contact point temperature measurement. An additional heating source generated the required temperature differences.[34] All measurements were carried out at room temperature in air.

The thermal conductivity λ was measured with a Laser-Flash Analyzer LFA 1000 (Linseis Thermal Analysis, Selb, Germany) using a 10 mm × 10 mm sample. For this purpose, Al_2O_3 substrates (635 μm) coated with a Bi_2Te_3 film (14 μm) as well as uncoated Al_2O_3 were measured. Therefore, the samples were first covered with a thin graphite layer and measured in a graphite sample holder in vacuum at room temperature. First, the uncoated Al_2O_3 substrate was measured and the thermal conductivity was determined. Using the measured thermal conductivity of Al_2O_3 and the two-layer model according to Dusza, a second measurement of the Bi_2Te_3-coated Al_2O_3 was performed, allowing the evaluation of the thermal conductivity of the Bi_2Te_3 film.[35]

Based on the determined thermoelectric properties, both the power factor

$$PF = \sigma S^2 \tag{1}$$

and the figure of merit

$$ZT = (\sigma S^2 T)/\lambda \tag{2}$$

were determined. The power factor PF is often used as a measure of the energy production of a thermoelectric material, while the thermoelectric figure of merit ZT describes the efficiency of a thermoelectric material.[36,37]
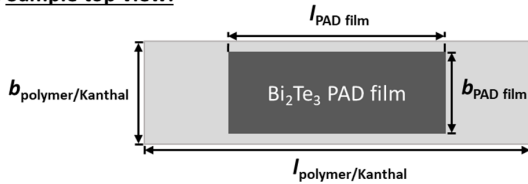
2.4. Thermoelectric Behavior during Bending

Elastic and electrically insulating Mylar and Kapton foils with thicknesses of 100 μm each were selected as substrate materials for thermoelectric measurements under bending. As both were self-adhesive, they were bonded to bendable (metallic) Kanthal foils with a thickness of 100 μm prior to the deposition of Bi_2Te_3 films. A schematic representation of the sample is shown in **Figure 3**.

A rectangular area of 10 mm × 25 mm of Bi_2Te_3 was deposited on each substrate with the assistance of masking. Both the electrical conductivity and the Seebeck coefficient before bending and after bending, as well as during bending, were measured on a specifically designed setup, as shown in **Figure 4**.

The samples were placed on a 3D-printed radius and were bent convexly. Before measuring the thermoelectric properties, the samples were fixed at the edges using adhesive strips. Along the short side of the sample, an electrical contact was established over the entire width ($b_{PAD\ film}$) of the sample. These two contacts were connected to a Keithley 2400 SourceMeter, allowing a constant current I to be impressed. The circuit included a switch. The current was only impressed during the measurement of the electrical conductivity. In the case of a closed switch, the modulation heater was deactivated, which is why there was no temperature difference at the two punctiform Au–Pt thermocouples connected on the surface of

**ADVANCED
SCIENCE NEWS**
www.advancedsciencenews.com

Energy Technology
Generation, Conversion, Storage, Distribution
www.entechnol.de

(a) **Sample top view:**
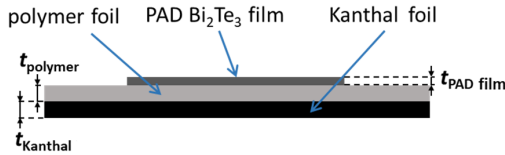

(b) **Sample cross-section:**

Figure 3. Schematic representation of the sample. a) Top view of the polymer foil ($l_{\text{Kanthal/polymer}} = 50\,\text{mm}$, $b_{\text{Kanthal/polymer}} = 12\,\text{mm}$) with a rectangular Bi_2Te_3 PAD film ($b_{\text{PAD film}} = 10\,\text{mm}$, $l_{\text{PAD film}}$ 25 mm). b) Cross section of the sample with a Kanthal and polymer foil of the same thickness ($t_{\text{Kanthal}} = t_{\text{polymer}} = 100\,\mu\text{m}$) and a Bi_2Te_3 film with variable process-depending thicknesses ($t_{\text{PAD film}}$).

the Bi_2Te_3 films. The voltage drop U_σ between the thermocouples with a distance of $s = 10\,\text{mm}$ was measured via the two platinum leads of the thermocouples with a Keithley 2700 Digital

(a) **Measurement setup top view:**
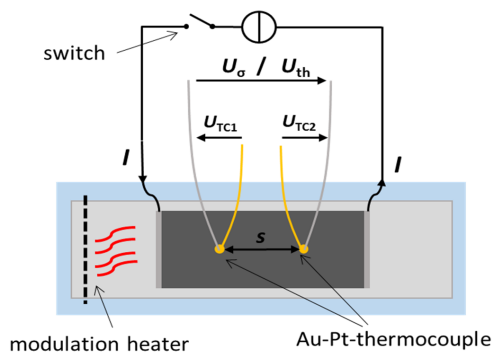
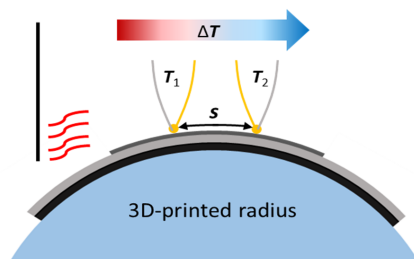(b) **Measurement setup cross-section:**

Figure 4. Measurement setup for the thermoelectric characterization of the PAD films during bending and in the planar state. a) Top view of the measurement setup including electrical connections with a switch to measure either the electrical conductivity or the Seebeck coefficient. The modulation heater is only activated if the switch is turned off. b) Cross section of the measurement setup during bending with the thermocouple spacing $s = 10\,\text{mm}$.

Multimeter. Using the impressed current I and the measured voltage U_σ, the electrical conductivity σ of the sample was calculated. In Equation (3), $b_{\text{PAD film}}$ is the width of the films, $t_{\text{PAD film}}$ denotes the thickness, and s stands for the inner electrode, respectively, of the thermocouple spacing.

$$\sigma = \frac{s}{b_{\text{PAD film}} \cdot t_{\text{PAD film}}} \cdot \frac{I}{U_\sigma} \tag{3}$$

To determine the Seebeck coefficient S, the circuit was opened and an external modulation heater was activated near one side of the sample, leading to a temperature difference ΔT between the thermocouples. Due to this temperature difference, the thermoelectric voltage U_{th} was measured between the platinum wires of the thermocouples. From the measured thermoelectric voltage U_{th} and the contact point temperatures T_1 and T_2, determined from the thermoelectric voltages of the thermocouples U_{TC1} and U_{TC2}, the uncorrected Seebeck coefficient $S_{\text{uncorrected}}$ of the Bi_2Te_3 films was determined using Equation (4).[38]

$$S_{\text{uncorrected}} = \frac{U_{\text{th}}}{\Delta T} \tag{4}$$

$$S_{\text{sample}} = S_{\text{Pt}} - S_{\text{uncorrected}} \tag{5}$$

The Seebeck coefficient S_{sample} of the Bi_2Te_3 film was then calculated from the uncorrected Seebeck coefficient and the absolute Seebeck coefficient S_{Pt} of the platinum wires according to Equation (5).[39] The heating power and thus the different temperature differences were modulated, as shown in the study by Rettig.[40] The bending radii were varied from 60 mm down to 10 mm.

2.5. Setup Design and Characterization of the Samples as TEGs

The patterns of the TEG were manufactured with the assistance of masking. First, four PAD films, the so-called thermoelectric legs, with a width of 3.5 mm and a length of 20 mm were deposited parallel to each other on a self-adhesive Kapton foil, which was adhered on a Kanthal sheet, both of 100 μm thickness. Four parallel Bi_2Te_3 legs were thermoelectrically connected in series using a copper wire. A scheme of the setup to characterize the planar PAD films as TEGs is shown in **Figure 5**.

At one end of the legs, an external heating element was added to generate a variable temperature gradient over the PAD films. With two Au–Pt thermocouples, the temperature differences between the hot and cold sides were measured. Their average value was also used to determine the operating temperature (T_{mean}) of the TEG. The circuit was closed by connecting the two outer legs via a resistor cascade, which acted as a variable load. Currents and voltages were recorded with a Keithley 2700 Digital Multimeter. As the copper wires also have a very small Seebeck coefficient of $S_{\text{copper}} = +1.83\,\mu\text{V}\,\text{K}^{-1}$, this was compensated for the characterization of the TEG.[41] For this purpose, the part of the thermoelectric voltage caused by copper was subtracted from the total measured voltage. The voltage–current and power–current characteristics of only Bi_2Te_3 films were then used to characterize the TEG. The TEGs was first measured in the unloaded (i.e., nonbent) state and then during bending. Eventually, its thermoelectric behavior
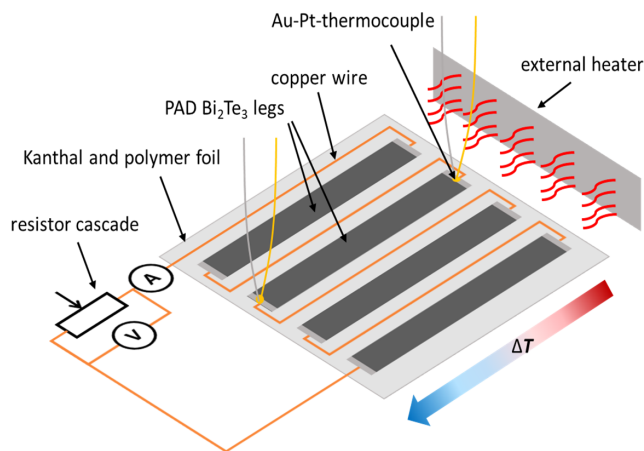
Figure 5. Schematic representation of the measurement setup for characterizing the PAD TEG. Four parallel Bi_2Te_3 legs were thermoelectrically connected in series using copper wire and heated on one side with an external heater. The load resistance was varied via a resistor cascade and the current as well as the voltage were recorded via a digital multimeter.

Figure 6. XRD pattern of Bi_2Te_3 powder and the Bi_2Te_3 PAD film compared with a Bi_2Te_3 reference 00-015-0863.

after bending was investigated. For the convex bending, 3D-printed radii were used and the samples were fixated using adhesive strips.

3. Results and Discussion

3.1. Step 1: Deposition and Characterization on Alumina

3.1.1. Morphology and Crystallinity

The deposited Bi_2Te_3 films on Al_2O_3 substrates were first characterized by their XRD patterns. A comparison of the obtained powders with the films in the as-deposited state is shown in **Figure 6**, including a reference reflection pattern map of Bi_2Te_3.

The positions of the reflections of the used Bi_2Te_3 powder, of the PAD film, and of the reference agree well, which confirms that the PAD film is pure Bi_2Te_3. The widening of the reflection of the XRD pattern of the PAD film compared with the powder indicates a reduction of the crystallite size, which is a clear indication that the densification of the film follows the RTIC process. During deposition, the kinetic energy of the impacting particles is converted into fracture energy (due to the formation of many new surfaces in the nanosized-deposited crystallites) and hence, into consolidation and plastic deformation of previously deposited particles.[42] The crystallite size of the film got reduced to ≈ 30 nm, as determined by Rietveld refinement. This is in the typical range of 30–60 nm for PAD films.[32,43] The morphologies of the deposited PAD films were additionally investigated by the scanning electron microscope. **Figure 7**a shows a fracture image of a Bi_2Te_3 film on an Al_2O_3 substrate. Figure 7b shows the top view of the Bi_2Te_3 film surface.

Both Figure 7a,b show that homogeneous and dense films were obtained by the PAD process. Figure 7a details the fracture
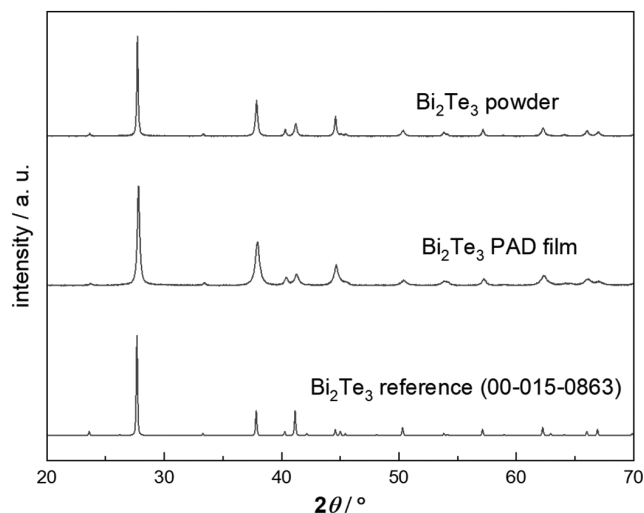
image with the good adherence of the Bi_2Te_3 film to the substrate due to the RTIC process. In addition, the fracture pattern shows a nanocrystalline dense film, as it is typical for PAD films and as it agrees with the crystallite size obtained by XRD. Compared with the mean particle size of $d_{50} = 6.42\,\mu m$ of the sieved starting powder, the particles became significantly smaller, which is a result of the RTIC process.[28–30] The surface of the film (Figure 7b) looks crater like, as it is typical for PAD films, and it is dense. In addition, Figure 7c shows a laser scanning microscope image of the surface of the Bi_2Te_3 film. It also shows the crater-like, dense film with a relatively homogeneous thickness. On the right side, the influence of masking can be seen. After removing the masking, the film has a clearly steep edge, which justifies the assumption of a rectangular cross section and the calculation of the electrical conductivity according to Equation (3). Thus, the PAD process can produce dense Bi_2Te_3 films directly from commercial Bi_2Te_3 powder without extensive pretreatment and with no post-treatment. It may be assumed that the PAD process can also be applied for doped Bi_2Te_3 (with even better thermoelectric properties), as doping should not affect the mechanical material properties, which are relevant for the deposition success.

3.1.2. Thermoelectric Characterization of the Bi_2Te_3 PAD Films on Alumina

To compare the thermoelectric properties of the deposited films with literature data, the thermoelectric properties on an alumina substrate were first used (details see Section 2.3). The results are summarized in **Table 1** and compared with spark plasma-sintered bulk samples, a common fabrication process for Bi_2Te_3.[44]

The electrical conductivity of the PAD film was determined to 29.8 S cm^{-1}, which is more than one decade lower than the spark plasma-sintered sample of Han et al.[44] The charge carrier
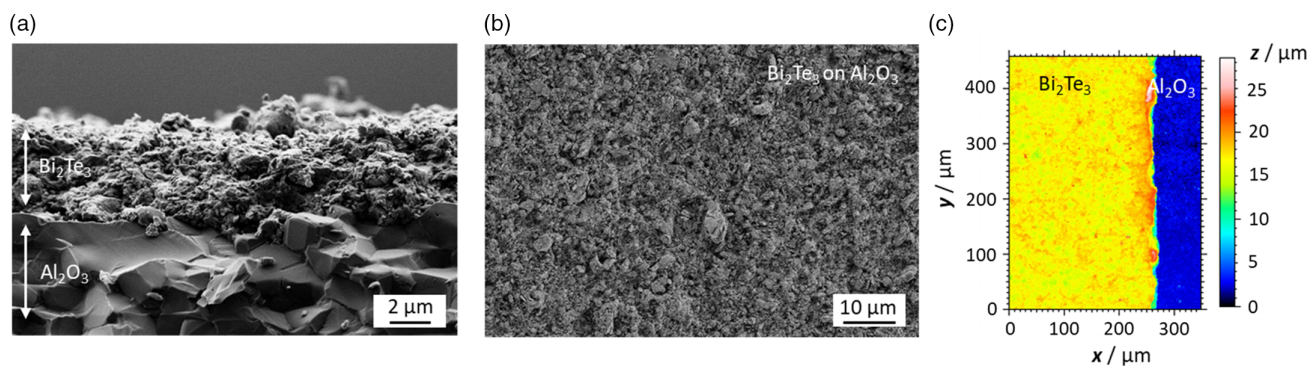
**ADVANCED
SCIENCE NEWS**

www.advancedsciencenews.com

Energy Technology
Generation, Conversion, Storage, Distribution

www.entechnol.de

Figure 7. SEM images: a) fracture image of a Bi_2Te_3 PAD film deposited on an Al_2O_3 substrate, b) top view of the Bi_2Te_3 PAD film, and c) laser scanning microscope image.

Table 1. Thermoelectric properties of a 14 µm-thick Bi_2Te_3 PAD film on Al_2O_3 compared with a spark plasma-sintered Bi_2Te_3 bulk sample.[44]

t [µm]	σ [S cm^{-1}]	n [cm^{-3}]	μ [cm^2 V^{-1} s^{-1}]	S [µV K^{-1}]	λ [W m^{-1} K^{-1}]	References
14	29.8	1.56×10^{19}	11.9	−145	0.12	This work
1000	307	1.2×10^{19}	354.9	−270	1.6	[44]

densities, however, do almost not differ ($1.56 \cdot 10^{19}$ vs. $1.2 \cdot 10^{19}$ cm^{-3}). Based on the measured charge carrier density and the electrical conductivity, a Hall mobility of $\mu_H = 11.9$ cm^2 V^{-1}s^{-1} can be derived for the PAD Bi_2Te_3 films. The lower conductivity can be explained by the low charge carrier mobility due to the enormous number of grain boundaries in the PAD film, a result of the PAD process. Figure 7 illustrates this. The lower electrical conductivity of PAD films has already been observed in previous studies and could even be increased by thermal annealing.[32] Similar results in the Hall mobility with p-doped Bi_2Te_3 PAD films were already observed by Baba et al.[45] The Seebeck coefficient of Bi_2Te_3 PAD films was determined to $S = -145$ µV K^{-1}. Compared with the spark plasma-sintered Bi_2Te_3, the absolute value is significantly lower. However, the deviation may have to do with the different tellurium content of the samples. Depending on the tellurium content, Bi_2Te_3 can even be an n- or a p-type material. The slightly higher charge carrier density and the lower Seebeck coefficient show that in this work, the tellurium content must be >0.6 mol%.[14] A major advantage of PAD films, especially for thermoelectric applications, is the low thermal conductivity of $\lambda = 0.12$ W m^{-1} K^{-1}, which is more than 10 times lower than typical Bi_2Te_3 bulk samples.[44] Compared with the calculated thermal conductivity of Baba et al. of a $t > 2$ mm PAD Bi_2Te_3 film with $\lambda \approx 0.5$ W m^{-1} K^{-1}, the here-derived thermal conductivity is even lower (approximately by a factor of 4).[45] The advantage of low thermal conductivity is the increased thermal resistance of the film, which allows a larger temperature to drop along the film without a thermal shunt current. The origin of the lower thermal conductivity is provisionally assigned to the huge number of blocking grain boundaries, which affect not only the electrical

conductivity but also the thermal conductivity. However, this has to be evaluated in detail and is not topic of this study. From the above-reported thermoelectric data, a figure of merit ZT for the PAD-deposited Bi_2Te_3 films of $ZT = 0.16$ at room temperature can be deduced (Equation (2)), Compared with literature, which gives a figure of merit ZT for bulk samples between 0.6 and 1.[46] This efficiency is still below the expectations, but it should be considered that in this work 99.9% pure commercial powder was used without any doping optimizations, and the manufacturing process consisted only of drying and of one sieving step. No thermal post-treatment was applied.

3.2. Step 3: Thermoelectric Behavior Before, During, and After Bending

3.2.1. Single Bending

The measured Seebeck coefficients and electrical conductivities of the PAD Bi_2Te_3 films on different polymer substrates before, during, and after bending are shown in **Figure 8**. In the left part, the results for the material combination "Kanthal–Kapton–Bi_2Te_3" are plotted (Figure 8a,c), whereas the right part shows the results of the system "Kanthal–Mylar–Bi_2Te_3" (Figure 8b,d). Data from different radii are separated by vertical dashed lines. In addition, the resulting PAD film thicknesses are given. Neither depending on the substrate material or on the film thickness nor on the bending radius, a Seebeck coefficient of −150 µV K^{-1} ± 10% was determined (±10% highlighted in blue). This also agrees with the data of Bi_2Te_3 on Al_2O_3 in Table 1. In the field of thermoelectrics, measurement deviations of ±5% can be expected at room temperature even with highly optimized measurement setups.[47] Even commercial measuring device manufacturers state a measuring accuracy of the Seebeck coefficient of ±7%.[48,49] As the Seebeck coefficient is a material property that does neither depend on the sample geometry nor on their density or their morphology, such a result could have been expected and was also shown for other thermoelectric materials.[50,51] The derived Seebeck coefficient data of the bending experiments hint to the fact that regardless of the film thickness and the bending radius, no
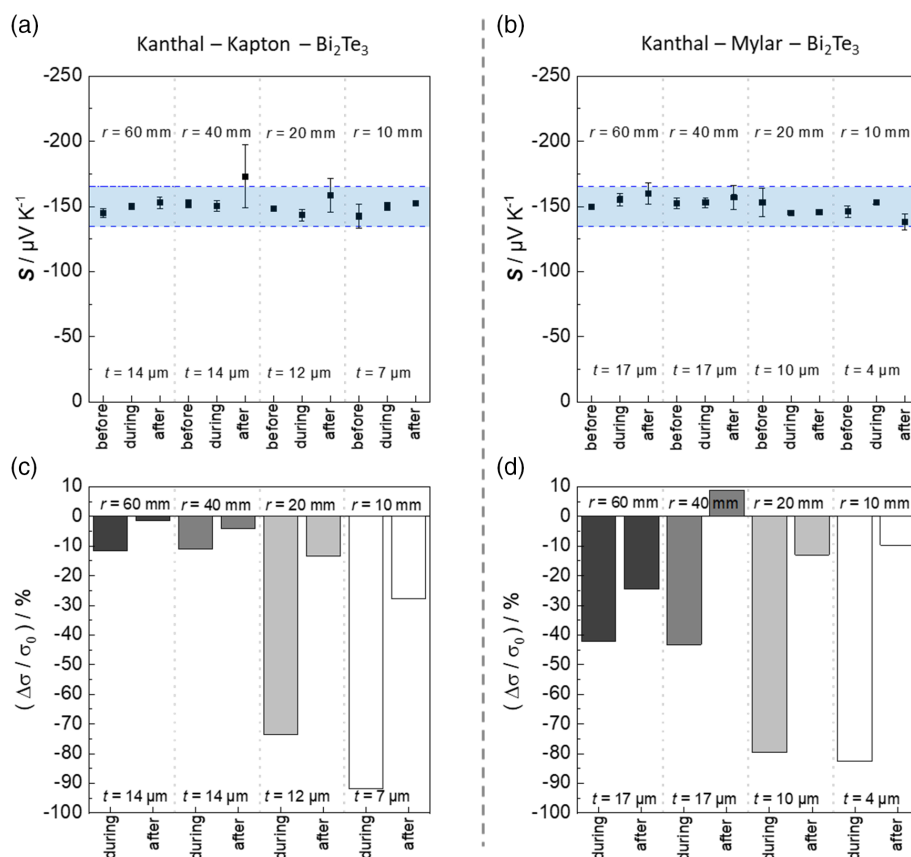
Figure 8. Seebeck coefficient and electrical conductivity of Bi_2Te_3 films before, during, and after bending over different convex radii. a) Seebeck coefficient of the films on Kanthal and Kapton. b) Seebeck coefficient of the films on Kanthal and Mylar. c) Relative conductivity change of the films on Kanthal and Kapton. d) Relative conductivity change of the films on Kanthal and Mylar.

continuous cracks form across the entire width of the Bi_2Te_3 film, as otherwise an insulating behavior should have been observed and Seebeck coefficients could not have been measured anymore.

Figure 8c,d shows the relative conductivity changes during and after bending normalized to the initial conductivity. Looking first at the electrical conductivity of the Bi_2Te_3 PAD film on Kanthal–Kapton, only a slight reduction of the conductivity of 10% up to bending over a convex radius of 40 mm can be observed. During bending over radii of 20 and 10 mm, large reductions of the conductivity by over 70% and 90%, respectively, can be seen. However, Figure 8c also shows that they are partially reversible. After bending over a 20 mm radius, the conductivity measured in the planar state decreases to 15% of the initial conductivity and to 25% for a 10 mm radius. A partially reversible behavior can also be observed in the conductivity measurements of the Bi_2Te_3 films on Kanthal–Mylar (Figure 8d). Here, bending over a 60 mm radius affects the conductivity almost that strong than bending over smaller radii. However, as the measurements each involve only one sample and are not a statistical series of experiments, the low partial reversibility of the electrical conductivity at the largest radius may be classified as a one-time effect, as even after bending smaller radii, the reversibility of the conductivity is higher. The measurements during bending already show a conductivity reduction of more than 40% at a radius

of 60 and 40 mm, which is significant compared with the data from Figure 8c. The results for radii of 20 and 10 mm are comparable, with conductivity decreases by 80%. A possible explanation of the only partially reversible behavior may be given with the help of **Figure 9**.

The partially reversible electrical conductivity behavior including the conductivity decrease during bending suggests that the nanocrystalline structure of the PAD Bi_2Te_3 film slowly forms cracks from the outside to the inside. As Figure 9a depicts, cracks of the film may form along the grain boundaries, resulting in an effectively smaller sample cross section and thus an apparently lower electrical conductivity. When recovered from bending, that is, in the nonbent planar state, the conductivity is partially restored, as the contacts between the separated grain boundaries are closed again. The nonreversible part of the conductivity measurements could be explained by partially spalled particles during bending or by nonclosing cracks due to the brittle material behavior.

Figure 10 shows an optical microscope image of a Bi_2Te_3 PAD film on Kapton before and after bending. Before bending, no abnormalities occur (Figure 10a). After bending over a radius of 20 mm, the sample has many small holes (Figure 10b), which underlines the suggestion of spalling particles or agglomerates during bending. Figure 10c additionally shows a Bi_2Te_3 PAD film
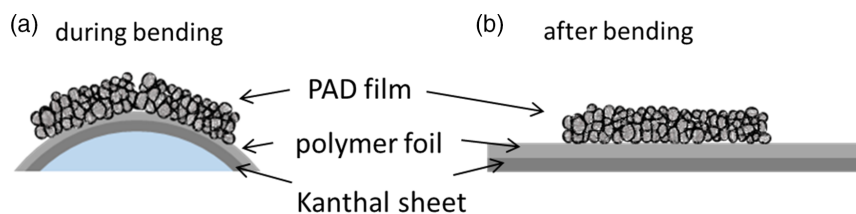
Figure 9. Suggestion, why the conductivity changes partially reversibly during and after bending. a) Cross section of a nanocrystalline PAD film during bending with small cracks, probably along grain boundaries. b) PAD film after bending: cracks are closed and electrical contacts are restored.
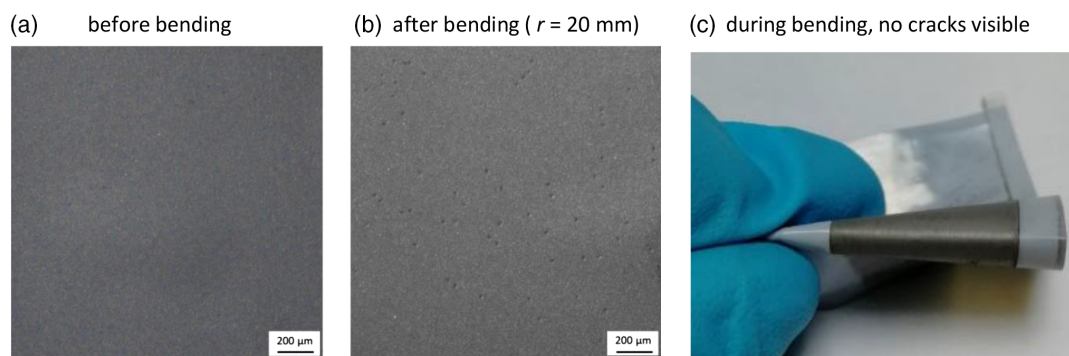

Figure 10. Images of Bi_2Te_3 films on Kapton: a) optical microscope image before bending, b) optical microscope image after bending with partially peeled off areas, and c) film bent by hand showing the good film adhesion.

on Kapton, which is being bent by hand. Even during the exposure, no cracks of the films are visible and the film adheres well. Also, no cracks could be observed under the microscope during bending, which on the one hand could be due to the more complicated focusing conditions under the microscope and on the other hand supports the assumption that very fine microcracks occur, as sketched in Figure 9.

3.2.2. Multiple Bending

In this section, the influence of multiple bending on the electrical conductivity as well as on the Seebeck coefficient will be investigated. For this purpose, the sample is measured in the nonbent planar state, then bent convexly over a radius up to 20 times, and then measured again in the planar state. The measurements were carried out under different radii, whereby each radius was assigned to a sample. The measurement results for both material configurations are shown in **Figure 11**.

The Seebeck coefficients after being bent n-times ($n_{max} = 20$) over different radii are given in Figure 11a,b for both substrate combinations, Kanthal–Kapton and Kanthal–Mylar, respectively. Regardless of the material combination and the number of bendings, the Seebeck coefficient remains almost unaffected with a value of $-150 \mu V K^{-1} \pm 10\%$. In Figure 11c,d, the relative conductivity changes after being bent are presented. At first glance, the measurements with the Bi_2Te_3–Kapton–Kanthal combination behave similarly, not depending on the bending radius of 60, 20, or 10 mm (Figure 11c). After the first bend, the conductivity hardly changes. Between the first and the tenth bend, the conductivity starts to decrease. After 20 bendings, the electrical

conductivity decreases by about 15%. At first glance, there appears to be a more significant decrease in conductivity at a radius of 40 mm (compared with 20 mm). However, the relative change after the first and the 20th bend is also only 15%. It can therefore be assumed that a somewhat larger agglomerate may already have flaked off during the first bend, which is why the electrical conductivity already drops significantly after the first bend. All in all, the measurements on Kanthal–Kapton show a behavior independent of the bending radius with conductivity changes of only 15% after 20 bendings.

Figure 11d also shows the results of the Kanthal–Mylar–Bi_2Te_3 combination. Unlike Kapton, this constellation shows a significant deterioration with increasing bending radius. At a radius $r < 20$ mm, the electrical conductivity already decreased by 40% after the 20th bend. A look at the different thicknesses of both systems shows that the thickness of the sample in the case of the Bi_2Te_3 film on Mylar is even somewhat smaller and can therefore not be the decisive point for this difference. Accordingly, the differences may be caused by the substrate. Different Young's moduli of the substrates provide for different stress transfers during bending ($E_{Mylar} \approx 3.8$ MPa; $E_{Kapton} \approx 5.5$ MPa).[52,53] Furthermore, it should be considered that both are self-adhesive films and therefore the adhesive layer will also have an influence on the mechanical stresses in the Bi_2Te_3 film. In our case, it seems that the Kapton foil reduces the effective bending stress better during convex bending. Due to the positive results and the bendability of the PAD films, no further experiments have been carried out in this direction. All in all, the results of the Kanthal–Kapton constellation are promising, especially for use as flexible TEGs.
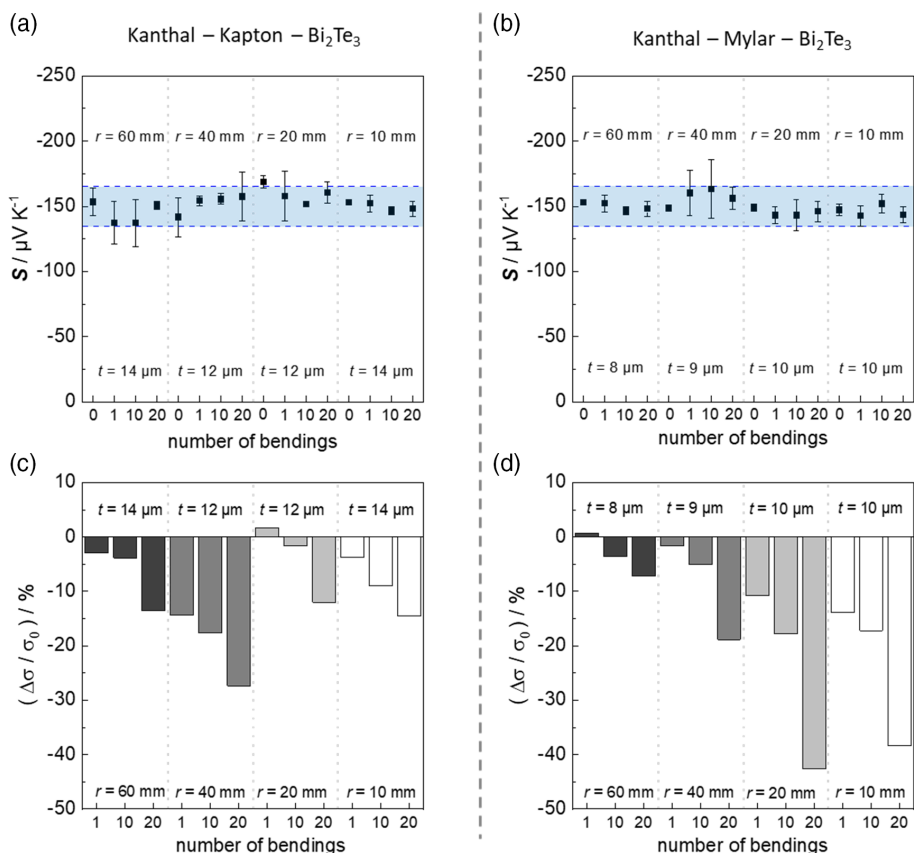
Figure 11. Seebeck coefficients and conductivities after being bent n-times over four different radii. a,b) Seebeck coefficients of Bi_2Te_3 on Kanthal–Kapton and Kanthal–Mylar, respectively. Highlighted in blue: expected Seebeck coefficient of $-150\,\mu V\,K^{-1} \pm 10\%$. c,d) Relative conductivity change.
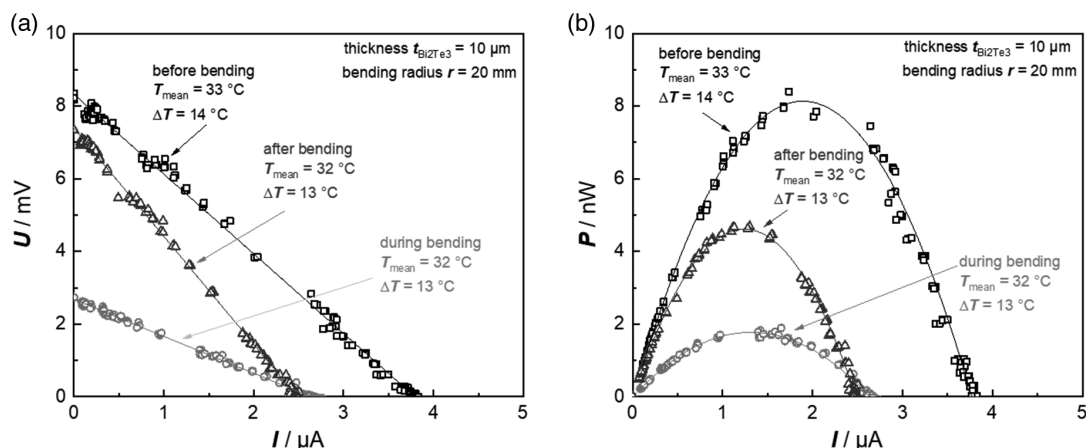

Figure 12. Characterization of a unileg TEG on Kanthal–Kapton. a) Voltage–current characteristic before, during, and after bending. b) Power–current characteristic before, during, and after bending.

3.3. Step5: Characterization of the Flexible TEGs Before, During, and After Bending

After measuring the thermoelectric properties of Bi_2Te_3 on Kanthal–Kapton during bending, a thermoelectric unileg generator as described in Section 2.5 with four legs was investigated at room temperature. The results are plotted in **Figure 12**.

In Figure 12a, the voltage–current characteristic and in Figure 12b the power–current characteristic of the processed Bi_2Te_3-based TEGs are plotted, before, during, and after convex bending over a radius of 20 mm at a mean temperature of

$T_{mean} = 32/33\,°C$ and a temperature difference of $\Delta T = 13/14\,°C$ between the hot and the cold side. In the planar state, the TEGs show an open-circuit voltage of about $U_0 = 8\,mV$. At a temperature gradient of $14\,°C$, this corresponds to an average Seebeck coefficient of each thermocouple of about $S = -143\,\mu V\,K^{-1}$, which is in good agreement with the results derived earlier. Under these conditions, a power of $P_{MPP} \approx 8\,nW$ can be generated in the maximum power point (MPP). During bending, the maximum obtainable power decreases to only $P_{MPP} = 2\,nW$. The lower short-circuit current ($U = 0$) and the lower open-circuit voltage ($I = 0$) can also be clearly seen. The significantly lower short-circuit current can be explained by decreased conductivity of the legs during bending that results in a higher internal resistance. A similar behavior has already been observed in Figure 8c. For the open-circuit voltage, a bending-independent behavior was expected, as shown in Section 4.2.1. With a temperature difference between the warm and cold sides of $13\,°C$, a thermoelectric voltage of only $U_0 = 2.8\,mV$ is achieved. Considering the number of legs and the temperature difference, this results in a Seebeck coefficient of only $S = -54\,\mu V\,K^{-1}$. This behavior cannot be explained so far. After bending, the open-circuit voltage increases again to the expected initial state and matches the results measured several times before. However, it can also be clearly seen here that the TEG was permanently deteriorated. In the MPP, only about $P_{MPP} = 5\,nW$ can be harvested. This is due to the larger internal resistance, also indicated by the lower slope. This is consistent with the decreased conductivity described earlier. Nevertheless, it was shown that the PAD process could produce a planar Bi_2Te_3-TEG on polymer films that exhibited partially reversible behavior even after bending. This work provides a basis for future research projects and offers a promising method to manufacture flexible planar TEGs on polymer films, due to the short powder preparation time and no postprocessing.

4. Summary

In this work, it was successfully demonstrated that the deposition of commercial Bi_2Te_3 powder on Al_2O_3, Mylar, and Kapton is possible using the PAD method. During this process nanocrystalline well-adhered films are formed (SEM images) without any crystal phase changes of the material during the PAD process. While the Seebeck coefficients remain unaffected independently on the substrate and on the bending radius, the electrical conductivity decreases compared with bulk material. It is assumed that large number of grain boundaries that exist due to the nanocrystallinity of the films are barriers for the charge carrier transport. They also hinder phonon movement, which leads to the positive effect of lower thermal conductivity. Furthermore, thin thermoelectric PAD films can be bent.

Both the electrical conductivity and the Seebeck coefficient were measured before, during, and after bending at different radii. It was found out that down to a radius of $40\,mm$, hardly any change in electrical conductivity could be measured on Kanthal–Kapton. At stronger bending, the conductivity decreased during bending, but the conductivity recovered partially. The Seebeck coefficient was neither affected by the bending radii nor by the number of bendings.

A first flexible thermoelectric unileg generator with four thermocouples of PAD Bi_2Te_3 films was fabricated by PAD. During bending, the thermoelectric properties decreased; however, they again recovered partially. Thus, the PAD process and the nanocrystalline structure not only provide lower thermal conductivity but also allow for the combination of Bi_2Te_3 and polymers without additional thermal treatment for the use as flexible planar TEGs.

Conflict of Interest

The authors declare no conflict of interest.

Author Contributions

R.W. and J.S.M. contributed equally to this work. R.W., J.S.M., D.S.-K., and R.M. conceived the experiments. R.W. and J.S.M. developed the measurement setups. J.S.M. performed the experiments. All authors analyzed the data, evaluated and discussed the results, and wrote the paper.

Data Availability Statement

The data that support the findings of this study are available from the corresponding author upon reasonable request.

[1] E. Garofalo, M. Bevione, L. Cecchini, F. Mattiussi, A. Chiolerio, *Energy Technol.* **2020**, *8*, 2000413.

[2] H. Jouhara, N. Khordehgah, S. Almahmoud, B. Delpech, A. Chauhan, S. A. Tassou, *Therm. Sci. Eng. Prog.* **2018**, *6*, 268.

[3] N. Jaziri, A. Boughamoura, J. Müller, B. Mezghani, F. Tounsi, M. Ismail, *Energy Rep.* **2020**, *6*, 264.

[4] D. Enescu, in *Green Energy Advances* (Ed: D. Enescu), IntechOpen London, United Kingdom **2019**.

[5] R. M. Ambrosi, H. Williams, E. J. Watkinson, A. Barco, R. Mesalam, T. Crawford, C. Bicknell, P. Samara-Ratna, D. Vernon, N. Bannister, D. Ross, J. Sykes, M.-C. Perkinson, C. Burgess, C. Stroud, S. Gibson, A. Godfrey, R. G. Slater, M. J. Reece, K. Chen, K. Simpson, R. Tuley, M. Sarsfield, T. P. Tinsley, K. Stephenson, D. Freis, J.-F. Vigier, R. J. M. Konings, C. Fongarland, M. Libessart, et al., *Space Sci. Rev.* **2019**, *215*, 1125.

**ADVANCED
SCIENCE NEWS**

www.advancedsciencenews.com

Energy Technology
Generation, Conversion, Storage, Distribution

www.entechnol.de

[6] Y. P. Prilepo, A. A. Pustovalov, V. V. Sinyavskiy, N. M. Sudak, O. B. Yatsenko, *Therm. Eng.* **2012**, *59*, 981.

[7] D. M. Rowe, *Appl. Energy* **1991**, *40*, 241.

[8] N. Espinosa, M. Lazard, L. Aixala, H. Scherrer, *J. Electron. Mater.* **2010**, *39*, 1446.

[9] M. Kober, T. Knobelspies, A. Rossello, L. Heber, *J. Electron. Mater.* **2020**, *49*, 2902.

[10] X. Liu, Y. D. Deng, K. Zhang, M. Xu, Y. Xu, C. Q. Su, *Appl. Therm. Eng.* **2014**, *71*, 364.

[11] Y. Zhang, M. Cleary, X. Wang, N. Kempf, L. Schoensee, J. Yang, G. Joshi, L. Meda, *Energy Convers. Manage.* **2015**, *105*, 946.

[12] A. Nozariasbmarz, H. Collins, K. Dsouza, M. H. Polash, M. Hosseini, M. Hyland, J. Liu, A. Malhotra, F. M. Ortiz, F. Mohaddes, V. P. Ramesh, Y. Sargolzaeiaval, N. Snouwaert, M. C. Özturk, D. Vashaee, *Appl. Energy* **2020**, *258*, 114069.

[13] G. J. Snyder, E. S. Toberer, *Nat. Mater.* **2008**, *7*, 105.

[14] I. T. Witting, T. C. Chasapis, F. Ricci, M. Peters, N. A. Heinz, G. Hautier, G. J. Snyder, *Adv. Electron. Mater.* **2019**, *5*, 1800904.

[15] H. Lee, *Thermoelectrics, Design and Materials*, Wiley, Chichester, West Sussex **2017**.

[16] J.-H. Bahk, H. Fang, K. Yazawa, A. Shakouri, *J. Mater. Chem. C* **2015**, *3*, 10362.

[17] Y. Du, K. F. Cai, S. Z. Shen, R. Donelsonand, J. Y. Xu, H. X. Wang, T. Lin, *RSC Adv.* **2017**, *7*, 43737.

[18] Y. Du, K. Cai, S. Chen, H. Wang, S. Z. Shen, R. Donelson, T. Lin, *Sci. Rep.* **2015**, *5*, 6411.

[19] C. S. Kim, H. M. Yang, J. Lee, G. S. Lee, H. Choi, Y. J. Kim, S. H. Lim, S. H. Cho, B. J. Cho, *ACS Energy Lett.* **2018**, *3*, 501.

[20] G. Lee, G. Choi, C. Kim, Y. Kim, H. Choi, S. Kim, H. Kim, W. Lee, B. Cho, *Appl. Sci.* **2017**, *7*, 1015.

[21] V. Leonov, in *Wearable Monitoring Systems* (Eds: V. A. Bonfiglio, D. de Rossi, Vol. *13*, Springer US., Boston, MA **2011**, p. 27.

[22] V. Leonov, T. Torfs, P. Fiorini, C. van Hoof, *IEEE Sens. J.* **2007**, *7*, 650.

[23] V. Leonov, R. J. M. Vullers, *J. Renewable Sustainable Energy* **2009**, *1*, 62701.

[24] H. Liu, Y. Wang, D. Mei, Y. Shi, Z. Chen, in *Wearable Sensors and Robots* (Eds: C. Yang, G. S. Virk, H. Yang), Vol. *399*, Springer Singapore, Singapore **2017**, p. 55.

[25] B. T. McGrail, A. Sehirlioglu, E. Pentzer, *Angew. Chem.* **2015**, *127*, 1730.

[26] I. Petsagkourakis, K. Tybrandt, X. Crispin, I. Ohkubo, N. Satoh, T. Mori, *Sci. Technol. Adv. Mater.* **2018**, *19*, 836.

[27] Y. Wang, L. Yang, X.-L. Shi, X. Shi, L. Chen, M. S. Dargusch, J. Zou, Z.-G. Chen, *Adv. Mater.* **2019**, *31*, 1807916.

[28] D. Hanft, J. Exner, M. Schubert, T. Stöcker, P. Fuierer, R. Moos, *J. Ceram. Sci. Tech.* **2015**, *6*, 147.

[29] J. Akedo, *J. Therm. Spray Tech.* **2008**, *17*, 181.

[30] M. Schubert, D. Hanft, T. Nazarenus, J. Exner, M. Schubert, P. Nieke, P. Glosse, N. Leupold, J. Kita, R. Moos, *Funct. Mater. Lett.* **2019**, *12*, 1930005.

[31] L. Paulatto, D. Fournier, M. Marangolo, M. Eddrief, P. Atkinson, M. Calandra, *Phys. Rev. B* **2020**, *101*, 205419.

[32] J. Exner, T. Nazarenus, D. Hanft, J. Kita, R. Moos, *Adv. Mater.* **2020**, *32*, 1908104.

[33] R. Werner, J. Kita, M. Gollner, F. Linseis, R. Moos, *J. Sens. Sens. Syst.* **2021**, *10*, 71.

[34] R. Werner, J. Kita, M. Gollner, F. Linseis, R. Moos, in *Proc. SMSI Nuremberg* AMA Service GmbH, Wunstorf/Germany **2021**, p. 77 https://doi.org/10.5162/SMSI2021/A6.2.

[35] L. Dusza, *Dissertation, Karlsruhe Institute of Technology*, August **1996**.

[36] W. Liu, H. S. Kim, Q. Jie, Z. Ren, *Scr. Mater.* **2016**, *111*, 3.

[37] G. J. Snyder, A. H. Snyder, *Energy Environ. Sci.* **2017**, *10*, 2280.

[38] Y.-G. Kim, K. S. Gam, K. H. Kang, *Sci. Instrum.* **1998**, *69*, 3577.

[39] J. P. Moore, R. S. Graves, *J. Appl. Phys.* **1973**, *44*, 1174.

[40] F. Rettig, R. Moos, *Sens. Actuators, B* **2007**, *123*, 413.

[41] N. Cusack, P. Kendall, *Proc. Phys. Soc.* **1958**, *72*, 898.

[42] J. Exner, M. Schubert, D. Hanft, J. Kita, R. Moos, *J. Eur. Ceram. Soc.* **2019**, *39*, 592.

[43] D. Hanft, J. Exner, R. Moos, *J. Power Sources* **2017**, *361*, 61.

[44] M.-K. Han, Y. Jin, D.-H. Lee, S.-J. Kim, *Materials* **2017**, *10*, 1235.

[45] S. Baba, L. Huang, H. Sato, R. Funahashi, J. Akedo, *J. Phys.: Conf. Ser.* **2012**, *379*, 12011.

[46] B. Chen, M. Kruse, B. Xu, R. Tutika, W. Zheng, M. D. Bartlett, Y. Wu, J. C. Claussen, *Nanoscale* **2019**, *11*, 5222.

[47] N. D. Lowhorn, W. Wong-Ng, Z. Q. Lu, E. Thomas, M. Otani, M. Green, N. Dilley, J. Sharp, T. N. Tran, *Appl. Phys. A* **2009**, *96*, 511.

[48] *Linseis Thermal Analysis, Datasheet: LSR-3*, https://www.linseis.com/en/products/thermoelectrics/lsr-3/ (accessed: November 2021).

[49] *NETZSCH-Gerätebau GmbH, Datasheet: SBA 458 Nemesis*, https://www.netzsch-thermal-analysis.com/en/products-solutions/seebeck-coefficient-electrical-conductivity/sba-458-nemesis/ (accessed: November 2021).

[50] F. Rettig, R. Moos, *Semiconductor Gas Sensors* (Eds: R. Jaanis, O. K. Tan), Vol. *82*, Elsevier Amsterdam/Netherlands **2013**, p. 261 https://doi.org/10.1533/9780857098665.2.261.

[51] S. Bresch, B. Mieller, D. Schoenauer-Kamin, R. Moos, F. Giovanelli, T. Rabe, *J. Appl. Phys.* **2019**, *126*, 75102.

[52] *TAP Plastics, Datasheet: Polyester Film or Mylar Film Properties*, https://www.tapplastics.com/image/pdf/Prod%20Data-%20Polyester%20Film.pdf (accessed: October 2021).

[53] *DuPont, Datasheet: DuPont Kapton EN*, https://www.dupont.com/content/dam/dupont/amer/us/en/products/ei-transformation/documents/EI-10173-Kapton-EN-Data-Sheet.pdf (accessed: October 2021).